Research Article

Nano Research
2021, 14(5): 1488–1494

ISSN 1998-0124 CN 11-5974/O4
https://doi.org/10.1007/s12274-020-3207-9

Exciton recycling via InP quantum dot funnels for luminescent solar concentrators

Houman Bahmani Jalali[1,§], Sadra Sadeghi[2,§], Isinsu Baylam[3,4], Mertcan Han[5], Cleva W. Ow-Yang[6], Alphan Sennaroglu[3,4], and Sedat Nizamoglu[1,2,5] (✉)

[1] *Graduate School of Biomedical Sciences and Engineering, Koç University, Istanbul 34450, Turkey*
[2] *Graduate School of Material Science and Engineering, Koç University, Istanbul 34450, Turkey*
[3] *Koç University Surface Science and Technology Center (KUYTAM), Koç University, Istanbul 34450, Turkey*
[4] *Laser Research Laboratory, Koç University, Istanbul 34450, Turkey*
[5] *Department of Electrical and Electronics Engineering, Koç University, Istanbul 34450, Turkey*
[6] *Department of Material Science and Nano Engineering, Sabanci University, Istanbul 34956, Turkey*
[§] *Houman Bahmani Jalali and Sadra Sadeghi contributed equally to this work.*

Received: 6 August 2020 / **Revised:** 20 October 2020 / **Accepted:** 22 October 2020

ABSTRACT

Luminescent solar concentrators (LSC) absorb large-area solar radiation and guide down-converted emission to solar cells for electricity production. Quantum dots (QDs) have been widely engineered at device and quantum dot levels for LSCs. Here, we demonstrate cascaded energy transfer and exciton recycling at nanoassembly level for LSCs. The graded structure composed of different sized toxic-heavy-metal-free InP/ZnS core/shell QDs incorporated on copper doped InP QDs, facilitating exciton routing toward narrow band gap QDs at a high nonradiative energy transfer efficiency of 66%. At the final stage of non-radiative energy transfer, the photogenerated holes make ultrafast electronic transitions to copper-induced mid-gap states for radiative recombination in the near-infrared. The exciton recycling facilitates a photoluminescence quantum yield increase of 34% and 61% in comparison with semi-graded and ungraded energy profiles, respectively. Thanks to the suppressed reabsorption and enhanced photoluminescence quantum yield, the graded LSC achieved an optical quantum efficiency of 22.2%. Hence, engineering at nanoassembly level combined with nonradiative energy transfer and exciton funneling offer promise for efficient solar energy harvesting.

KEYWORDS

energy transfer, indium phosphide, quantum dot, light harvesting, luminescent solar concentrator, luminescent solar concentrators (LSC)

1 Introduction

The energy delivered by the Sun to the Earth in one hour (4.6×10^{20} Joules) is close to the global annual energy consumption [1]. Efficient collection of solar photons and subsequent conversion to electricity can significantly decrease the demand for fuel-based energy and lead to a clean and sustainable energy solution that can have positive impact on environment, economy, and health. For that, luminescent solar concentrators (LSCs) integrated with photovoltaics (PV) hold significant potential [2–6]. LSCs can advantageously absorb large-area sunlight, and the down-converted light is propagated by total internal reflection into the small-area edges, where light energy is converted into electrical energy by PVs cells [7, 8]. Due to the capability of large-area light harvesting and the use of small-area PVs, LSCs can reduce the operational cost of PVs and their turn-over time [9]. Moreover, LSCs utilized as semitransparent photovoltaic windows can be a viable solution for net-zero-energy buildings in urban areas [10].

Quantum dots hold significant promise for LSCs because of their beneficial properties, such as high quantum yield, good photostability and strong absorption [11, 12]. A variety of techniques at the quantum dot and device level were investigated to increase the external quantum efficiency (EQE) of LSCs [4, 10, 13–15]. At the quantum dot level, Type-II core/shell heterojunctions [16-18], layered hybrid metal halide perovskites [19], coordination engineered perovskites [20], indirect band gap quantum dots [21], alloyed quantum dots (QDs) [22], and QDs doped with transition-metal ions [23–25] were reported to suppress losses originating from reabsorption and increase photoluminescence quantum yield (PLQY). At the device level, direct incorporation of QDs into polymeric waveguides [6, 16, 17], doctor-blade deposition of quantum dots as single QD-layer [9] and tandem architectures [26, 27] have been reported for the development of low-loss LSCs.

In this study, we nanoengineered LSCs at quantum dot assembly level and formed toxic-heavy-metal-free band gap gradient to enhance the energy harvesting efficiency. The energy funnel directs photoexcited charge carriers from smaller-toward larger-sized InP-based QDs, which recombine radiatively in localized excited states of copper-doped InP-based QDs at the final stage of non-radiative energy transfer. The exciton

Address correspondence to snizamoglu@ku.edu.tr

recycling takes place by resonance transfer of both radiative excitons and trapped excitons from large-gap QD layer to small-gap QD layer. At the final step, the resulting near-IR emission is guided to the PV module for electricity generation (Fig. 1).

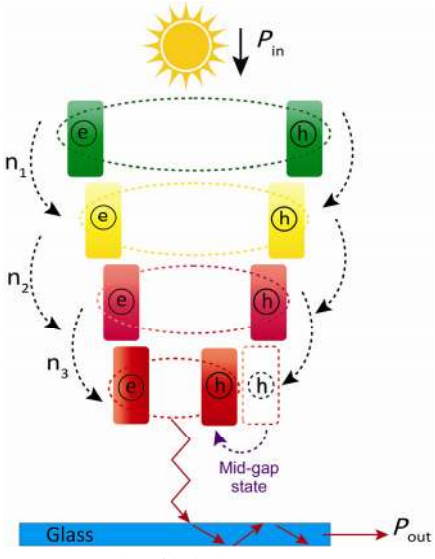

Figure 1 Design principle of light harvesting energy-gap gradient LSC using indium phosphide QDs. An LSC is composed of four layers of graded-gap InP QDs on a glass. The nonradiative energy transfer occurs from green-emitting to yellow-emitting (n_1), yellow-emitting to red-emitting (n_2), and red-emitting to near-IR emitting (n_3) InP QDs. Both radiative excitons and trapped excitons are resonantly transferred to luminescent state of the larger QDs that lead to the increase of the in-device PL efficiency. Solar irradiation (P_{in}) is absorbed by the luminophores (in our case, InP multilayers), down-converted to the near-IR emission, and waveguided to the edge of the LSC (P_{out}) for electricity production.

2 Results and discussion

As the construction blocks of the graded-gap nanoassembly, we synthesized InP core quantum dots surrounded by a ZnS shell (see the Electronic Supplementary Material (ESM)) for the detailed synthesis procedure). We initially formed InP cores using hot-injection method as we reported previously [16, 28–31], and potential traps due to surface dangling bonds of the InP core were partially passivated with zinc carboxylate [32]. 0.6 nm ZnS shell [28, 30, 31] was grown via thermal decomposition of zinc diethyldithiocarbamate to increase the quantum yield and confine the photogenerated excitons inside the core, since higher PLQY leads to more efficient nonradiative energy transfer due to the increase of the Förster radius (see Eqs. (1) and (2) [28, 33, 34], in which, E, R_0, R, κ^2, n, Φ_d, and J_{da} denote the nonradiative energy transfer efficiency, Förster radius, donor-acceptor distance, random dipole orientation factor (= 2/3) [28, 34], refractive index of the medium, PLQY of donor, and overlap of the donor emission and acceptor absorption band, respectively.). The existence of InP and ZnS crystal structures was proved by high resolution transmission electron microscopy (HR-TEM) imaging and spatial frequency analysis of the images by fast Fourier transform (FFT), generating pseudo-diffraction patterns (Figs. 2(d) and 2(e)) [29, 35]. The interplanar distance of 0.33 nm was seen in the HR-TEM image, which corresponds to the (111) plane of the cubic InP structure (Fig. 2(d)). Moreover, FFT analysis shows the existence of the (111), (311) and (400) crystal planes of InP (PDF Card: 00-013-0232) and (220) and (311) crystal planes of ZnS (PDF Card: 00-001-0792) in the InP/ZnS core/shell nanostructure (Fig. 2(e))

$$E = \frac{1}{1+\frac{R^6}{R_0^6}} \quad (1)$$

$$R_0 = \frac{(8.79\times10^{23})\kappa^2\Phi_d J_{da}}{n^4} \quad (2)$$

To tune the band gap of InP/ZnS core/shell QDs, the growth temperature was varied from 220 to 280 °C. Thus, the mean particle size was increased from 2.71 ± 0.29 to 3.29 ± 0.29 nm and 3.8 ± 0.66 nm for green-, yellow- and red-emitting InP/ZnS core/shell QDs, respectively (Figs. 2(f)–2(h)). Moreover, for the introduction of the mid-gap states, host InP cores were doped with copper ions using well-known thermal decomposition method [12, 36]. Previously, we have synthesized copper doped InP core QDs and optimized their synthesis parameters [12]. Then, the copper to indium ratio was set as 1:100 to achieve maximum PLQY [12]. For the copper-doped InP/ZnS core/shell QDs, the particle size is 3.9 nm (Fig. 2(i)), which is slightly higher than the red-emitting QDs, due to the incorporation of copper-ions into the lattice [36]. QDs showed an increase in absorption below their 1S-1S excitonic transition energies, due to additional electronic transitions at higher energy levels (Fig. 2(a)). The green-, yellow- and red-emitting quantum dots showed PL peaks at 2.39, 2.18 and 2.00 eV, respectively (Fig. 2(b)). Significant PL redshift and broadening occurred upon incorporation of copper into the InP QDs (Fig. 2(b)), which enabled a large Stokes shift above 600 meV, i.e. between the first excitonic absorption and photoluminescence peaks of copper-doped InP QDs (Fig. 2(c)).

To investigate the dynamics of the copper-induced hole acceptor state (Fig. 3(a)), we used an ultrafast pump-probe spectrometer and measured the non-linear absorption variation of QDs at picosecond time scales. In the experiments, free charge carriers were first generated by using a femtosecond pump pulse at 320 nm with a fluence of 240 μJ·cm^{-2} and the resulting change ΔA in the nonlinear absorbance spectrum ($\Delta A = A_{pumped} - A_{unpumped}$, A_{pumped} = absorbance spectrum of the pumped sample and $A_{unpumped}$ = small-signal absorbance spectrum) was measured by using a femtosecond white-light probe covering the 430–800 nm spectral window. Over a time interval of 3.8 ps, the peak wavelength of the ΔA spectrum for doped-QDs shifted from 547 to 568 nm, indicating an energy difference of 84 meV (Fig. 3(b)), due to the relaxation of the hot excitons down to the band edges [37]. The ultrafast transient evolution of the nonlinear absorbance up to a delay of 80 ps (Fig. 3(c)) features an initial growth time τ_g (τ_g = 3.3 and 2.4 ps in undoped and doped QDs, respectively) due to the relaxation of the hot excitons to the band edges, followed by a bi-exponential decay characterized by decay times τ_1 and τ_2. The decay times τ_1 and τ_2 describe fast decay due to intermediate trapping states, as observed in earlier studies [38, 39]. In addition, a third longer decay exists over ns time scales due to inter-band electron-hole recombination. The measured ultrafast transition decay times of copper-doped InP QDs (τ_1 = 2.5 ps, τ_2 = 35 ps) at the probe wavelength of 570 nm (Fig. 3(c)) show higher electronic transition rates in comparison with undoped InP QDs (τ_1 = 3.4 ps, τ_2 = 52 ps) (Fig. S1 in the ESM) due to copper-induced mid-gap states. The role of copper-induced mid-gap states in increasing the decay rates is further elucidated in the contour plots (Fig. S2 in the ESM), which show the variation of ΔA (nonlinear absorbance) as a function of the probe wavelength and probe delay. As can be seen from Fig. S2 in the ESM, both ultrafast decay components become shorter for the copper doped InP QDs due to the formation of the copper-induced mid-gap states.

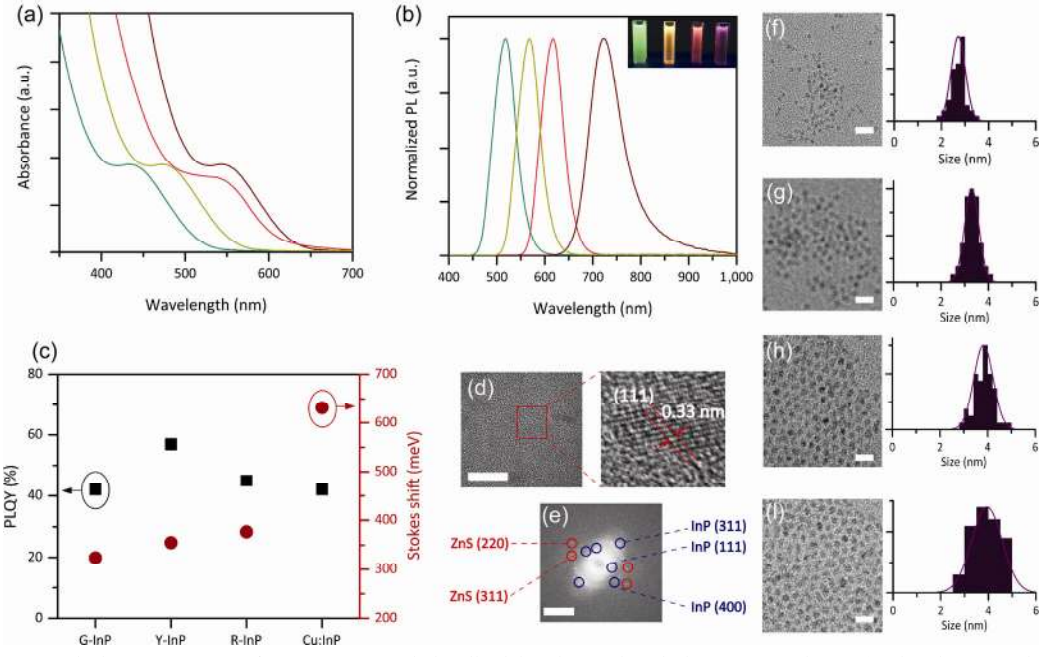

Figure 2 Synthesis and characterization of energy gap-graded colloidal indium phosphide quantum dots. (a) Absorbance and (b) normalized photoluminescence spectra of the colloidal green-, yellow-, red- and near-IR emitting InP/ZnS core/shell QDs. (Inset: Photograph of the colloidal green-, yellow-, red- and near-IR-emitting QDs under UV illumination). (c) PLQY and Stokes shift of the green-, yellow-, red- and near-IR emitting colloidal InP/ZnS core/shell QDs. (d) HR-TEM image of the red-emitting InP/ZnS (scale bar: 10 nm). (e) Spatial frequencies in the FFT of the HR-TEM image corresponding to InP and ZnS crystallographic planes (scale bar: 20 1/nm). Bright-field TEM images and corresponding particle size distribution of the (f) green- (2.71±0.29 nm), (g) yellow- (3.29±0.29 nm), (h) red- (3.82±0.40 nm), and (i) near-IR emitting (3.93±0.66 nm) InP/ZnS core/shell QDs (scale bars are 10 nm, minimum 100 particles were counted for the particle size distribution).

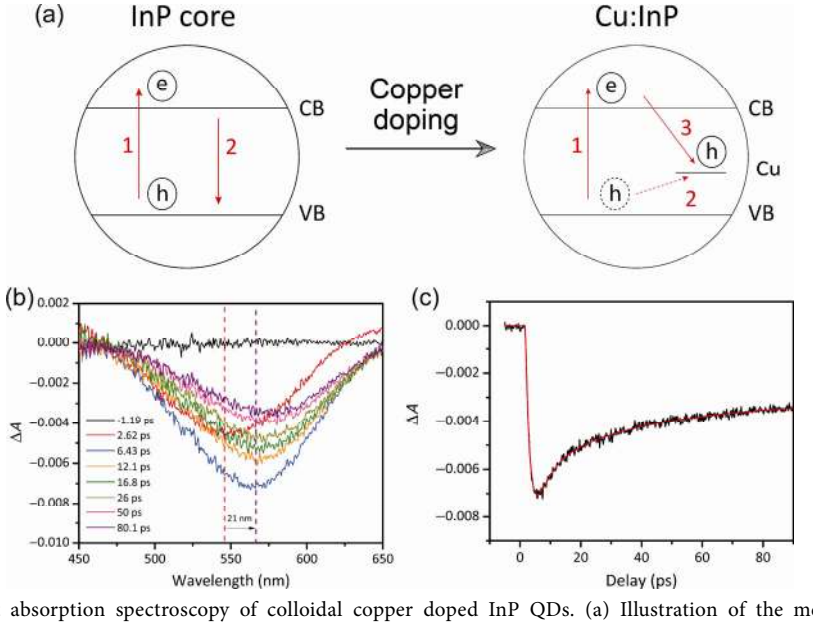

Figure 3 Ultrafast transient absorption spectroscopy of colloidal copper doped InP QDs. (a) Illustration of the mechanism of mid-gap state luminescence in Cu^{+} doped semiconductor QDs. Upon photoexcitation (1), the hole rapidly and non-radiatively localizes from the valence band to a Cu^{+} dopant to form a Cu^{2+} like ion (2). Radiative recombination of the electron from the conduction band with the copper-localized hole results in the emission of a photon (3). (b) The measured non-linear absorbance spectra of the copper doped InP QDs at eight selected probe delays ranging from −5 to 90 ps. The excitation wavelength was 320 nm. (c) Time-resolved variation of the nonlinear absorbance of the copper-doped InP QDs at the probe wavelength of 570 nm.

We constructed a graded-gap nanoassembly made of InP/ZnS core/shell QDs on a glass substrate. Layer-by-layer assembly has enabled the fabrication of graded nanoassemblies, i.e., the controlled assembly of layers of QDs, such that the layers have a gradation in energy gaps, as demonstrated in the fabrication of QD-based device applications ranging from solar cells [40–43] to biointerfaces [28]. Our QDs were assembled to produce an energy gap gradient from the top layer down to the substrate via spin-coating [28, 40, 44], starting from 2.38 eV emitting in the green and ending with 1.71 eV emitting in the near-IR, due to the copper states (Fig. 4(a), bottom panel). The thickness of each QD layer is determined to be around 14–24 nm according to our previous study [28].

To investigate the effect of energy transfer on optical properties, two different control groups, including semi-graded and ungraded nanoassemblies, were also fabricated (Fig. 4(a)). In the semi-graded device, three layers of red-emitting QDs were implemented on the Cu:InP/ZnS QDs (Fig. 4(a), middle panel)

and in the ungraded structure, all four layers consisted of Cu:InP/ZnS QDs (Fig. 4(a), top panel). The ungraded nanoassembly showed higher absorbance than the semi-graded and graded nanoassemblies, due to having more copper-doped InP QD layers, which have higher extinction coefficient in comparison with the other InP/ZnS core/shell quantum dots [45] (Fig. 4(b)). Moreover, the semi-graded nanoassembly has higher absorbance than graded nanoassembly due to the higher red-emitting layers. Device absorptance (η_{abs}) is defined as the ratio of the solar photons that are absorbed by the LSC fluorophores [10]; the device absorptance of the ungraded and semi-graded LSCs, which correspond to 5.16% and 5.03%, respectively, are higher than that of the graded LSC, which absorbs 4.91% of sunlight (Fig. 4(c)). Despite having lower absorbance, the graded nanoassembly shows significantly increased photoluminescence in the near-IR spectral region compared to inhomogeneously broadened PL of semi-graded and ungraded nanoassemblies (Fig. 4(d)). These results confirm exciton recycling in the narrow band-gap QD layer (i.e., Cu:InP/ZnS QD). The exciton recycling relies on two mechanisms: first, stepwise radiative exciton transfer from large-gap QD layers to small-gap QD layers and second, recovery of trapped excitons from large-gap QD layers to the small-gap QD layer [46]. In other words, electron-hole pairs trapped in defect states of the green-, yellow-, and red-emitting QD layers were recycled for eventual recombination in the Cu:InP/ZnS QD layer. Hence, the graded nanoassembly can emit with 61% stronger intensity, due to the super-efficient nonradiative energy transfer and exciton recycling effect. Moreover, the optical PL efficiency of nanoassemblies was measured in an integrating sphere (see the ESM) and showed a significant increase from 22.1% for the ungraded nanoassembly to 35.6% for the graded nanoassembly, due to implementation of a step-wise energy gradient profile and exciton recycling [28, 46–50] (Fig. 4(e)). We also studied time-resolved fluorescence dynamics of the graded nanoassembly using donor fluorescence lifetime in the absence of acceptors, and for that we fabricated a donor control group consisting of four layers of only green-emitting InP/ZnS QDs. Nanoassemblies were excited with a 375 nm pulsed laser, and their decay analyses were performed (Fig. 4(f)). The average lifetime (τ_{avg}) was calculated from an amplitude weighted mean [30] (Eq. (3)), and it decreased from 7.18 ns ± 0.34 (for the donor control group) to 2.41 ns ± 0.12 (the graded nanoassembly). The energy transfer efficiency was calculated based on Eq. (4) [51], in which τ_D and τ_{DA} were the donor lifetime of the donor control group and of the graded structure, respectively; the energy transfer efficiency corresponds to 66% for the graded architecture. This result shows that exciton accumulation in the Cu:InP/ZnS QDs is due to efficient nonradiative energy transfer. Because of enhanced emission characteristics and higher optical transmission, the graded nanoassembly is the best candidate for luminescent solar energy harvesting

$$\tau_{avg} = \frac{A_1\tau_1^2 + A_2\tau_2^2}{A_1\tau_1 + A_2\tau_2} \quad (3)$$

$$E = 1 - \frac{\tau_{da}}{\tau_d} \quad (4)$$

We constructed a graded-gap LSC on a commercial 6 cm × 6 cm × 2 mm glass substrate. The optical properties of the LSC were investigated to evaluate its suitability for solar energy harvesting. The LSC has a high- level of light transmission in the visible spectral window (Fig. 5(a)) that well suited for solar windows. In order to investigate the optical stability of the fabricated nano-assemblies, the PL efficiency of the device with graded architecture was measured at different time intervals

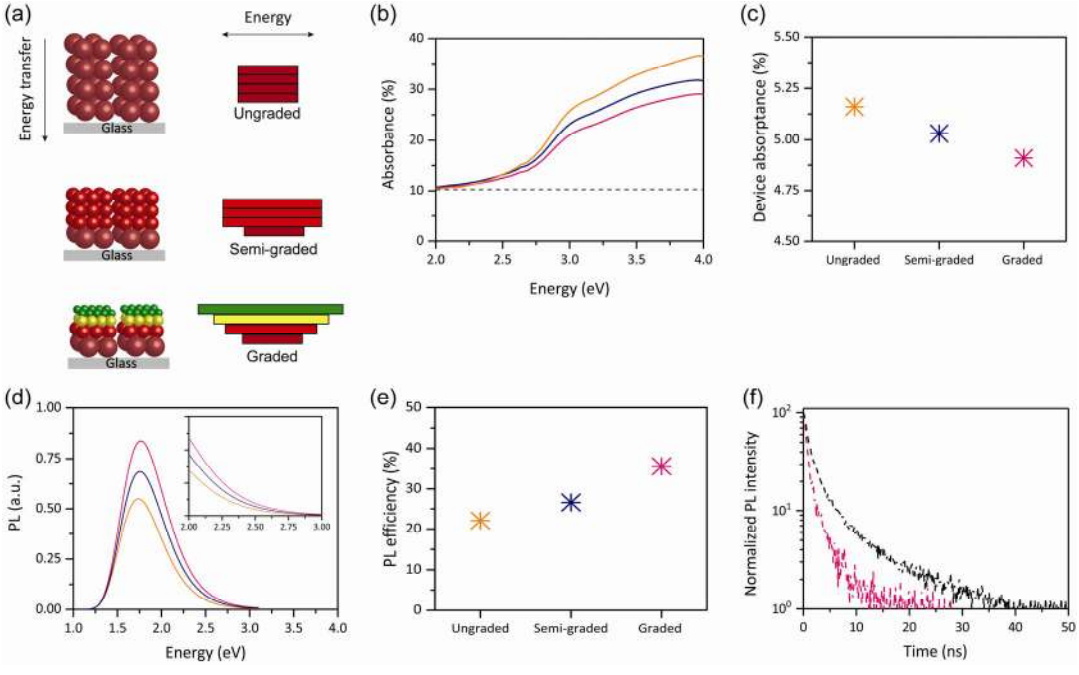

Figure 4 Steady-state and time-resolved optical characterizations of nanoassemblies. (a) Schematic representation of the fabricated ungraded, semi-graded and graded nanoassemblies. Ungraded structure consists of only copper-doped QD layers, semi-graded structure contains three red-emitting QD layers on copper-doped QD layer and graded structure has step-like energy gradient profile made of green-, yellow-, red- and near-IR emitting QDs. (b) Absorbance spectra of the graded (purple), semi-graded (blue) and ungraded (orange) structures on glass. Dashed line shows the offset due to light reflection from the front and back glass surfaces (~ 10% reflectivity). (c) Device absorptance of the graded (purple), semi-graded (blue) and ungraded (orange) nanoassemblies calculated according to the reference [10]. (d) Emission spectra of the graded (purple), semi-graded (blue) and ungraded (orange) nanoassemblies. Inset: Zoom-in of emission spectra of the graded (purple), semi-graded (blue) and ungraded (orange) nanoassemblies. (e) In-device PL efficiency of the ungraded, semi-graded and graded nanoassemblies. (f) Time-resolved PL spectra of the donor control group (black) and graded (purple) nanoassembly excited at 375 nm.

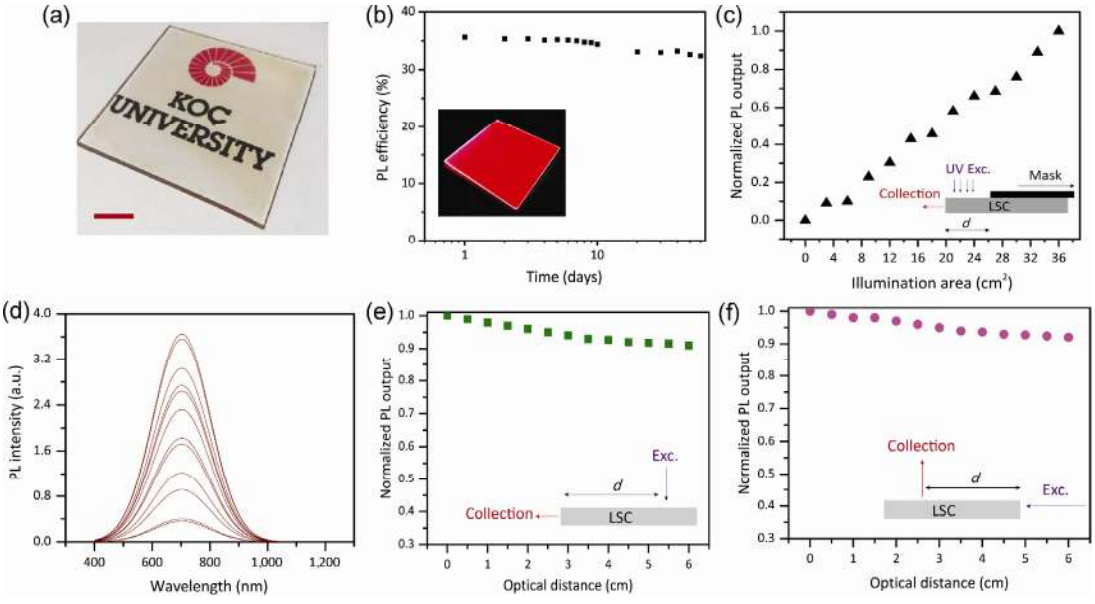

Figure 5 Optical characterization and performance analysis of the graded-gap LSC. (a) The transparency of the fabricated LSC was shown under ambient light (Scale bar is 2 cm). (b) The optical stability of the fabricated nano-assemblies. (inset: The photograph of the LSC under 365 nm ultraviolet irradiation. The total internal reflection is visible on the brighter edges). (c) The optical output intensity of the 6 cm × 6 cm × 2 mm LSC by changing the illumination area from 0 to 36 cm^2. (d) The output emission spectra of the 6 cm × 6 cm × 2 mm LSC by changing the illumination area from 0 to 36 cm^2 (Inset: Schematic of the setup to change the portion of the illuminated area of LSC under ultraviolet radiation). (e) The spectrally integrated light output of the LSC under the illumination by an ultraviolet laser beam at 500 nm wavelength. (Inset: The laser beam excitation was perpendicular to the surface and the light was collected from the slab edge at different optical distances). (f) The normalized PL output was shown at different optical distances ranging from 0 to 6 cm, when the laser beam with the wavelength of 500 nm was propagated inside the slab. (Inset: The schematic demonstrates the setup, in which the LSC is illuminated by the laser beam at the edge and the optical output was collected from the face by using an optical fiber).

during 60 days (Fig. 5(b)). It was demonstrated that the PL efficiency of the device only decreased from 35.6% to 32.4% (equal to ~ 8.9%) during 60 days, which confirmed the high optical stability of the fabricated LSC devices. The device was kept in the dark between the two consecutive PL efficiency measurements. The demonstrated optical stability of our devices is comparable to the previously reported studies, which showed a similar decreasing behavior in optical performance of the devices [19]. The brighter emission on the edges in comparison with surface shows optical waveguiding of the generated PL by LSC (Fig. 5(b) inset). As the illumination area increased from 0 to 36 cm^2 (equal to the full side length of 6 cm for the square-shaped LSC), the optical output intensity increased linearly, due to the effective suppression of the reabsorption by QDs (Fig. 5(c)). Meanwhile, the emission spectra of the QDs under different illumination areas showed no significant peak shift ($\Delta\lambda$ = 3 nm), demonstrating low reabsorption of the LSC under different areal illumination conditions (Fig. 5(d)). For further investigation of the reabsorption effect, the LSC was excited through the front surface by a laser light at 500 nm, and the light output intensity was recorded from the LSC edge at different optical distances from the excitation. The normalized integrated light intensity decreased only 9%, upon increasing the optical distance up to 6 cm (Fig. 5(e)). Moreover, the scattering measurement of the LSC was experimentally measured by propagating a laser beam of 500 nm wavelength through the LSC edge and collecting the output light at different optical distances from the illumination edge, by using an optical fiber positioned orthogonally to the beam direction. The normalized light output intensity decreased to 92% upon increase of the light collection distance up to 6 cm (Fig. 5(f)). These results show significant suppression of reabsorption via nonradiative energy transfer and low-loss propagation of photoluminescence.

The optical performance of graded luminescent solar concentrators was investigated. They were illuminated orthogonally to the front surface by a calibrated solar simulator of AM 1.5 G, and the photoluminescence generated by the QDs were coupled to the silicon solar cell positioned at the single collection edge. The EQE was calculated using the expression in Eq. (5), where I_{LSC} is the short-circuit current of the solar cell coupled to the LSC, when the LSC is illuminated by the solar simulator, I_{PV} is the short-circuit current of the solar cell, when the solar cell is directly illuminated by the solar simulator without the LSC. Based on the measurements, the EQE of the graded LSC was 1.68%. This efficiency level corresponds to a relative increase of 33.3%, compared to a semi-graded LSC having an EQE of 1.26%, due to the stepwise band-gap profiles in the graded LSC. To further increase the EQE level, nanoantennas that can harvest energy from thousands of donors to a single acceptor at molecular level and integration of back-reflectors or solar cells to all four edges of LSC can be utilized [12, 52]. Moreover, the optical quantum efficiency, which is defined as the fraction of the absorbed photons to the photons reaching to the output faces [10], corresponded to 22.2% (Eq. (S2) in the ESM). This is higher than the η_{OQE} of semi-graded LSC of 16.3%. Comparatively, the enhancement of optical quantum efficiency was higher than that of the external quantum efficiency, due to enhanced fluorescence efficiency while preserving lower absorptance [10].

$$\mathrm{EQE} = \frac{I_{LSC} \times A_{PV}}{I_{PV} \times A_{LSC}} \quad (5)$$

3 Conclusion

In summary, we have fabricated energy gradient QD nano-assemblies, based on InP/ZnS core/shell QDs emitting at green, yellow and red and copper-doped InP core/shell QDs emitting in the near-IR. The presence of the copper mid-gap states in the near-IR region was confirmed by ultrafast transient

absorption spectroscopy. The step-wise energy gradient architecture led strong exciton accumulation in the copper-doped InP/ZnS QDs, which facilitated significant optical quantum efficiency increase of LSCs due to the super-efficient energy transfer and exciton recycling. This work demonstrates that the strategy of nanoassembly engineering of QDs holds significant promise for efficient solar energy harvesting.

Acknowledgement

This project has received funding from the European Research Council (ERC) under the European Union Horizon 2020 Research and Innovation Programme (grant agreement no. 639846).

Electronic Supplementary Material: Supplementary material (QD synthesis procedure, device fabrication, optical characterization and performance analysis) is available in the online version of this article at https://doi.org/10.1007/s12274-020-3207-9.

References

[1] Crabtree, G. W.; Lewis, N. S. Solar energy conversion. *Phys. Today* **2007**, *60*, 37–42.

[2] Goetzberger, A.; Greube, W. Solar energy conversion with fluorescent collectors. *Appl. Phys.* **1977**, *14*, 123–139.

[3] Currie, M. J.; Mapel, J. K.; Heidel, T. D.; Goffri, S.; Baldo, M. A. High-efficiency organic solar concentrators for photovoltaics. *Science* **2008**, *321*, 226–228.

[4] Debije, M. G.; Verbunt, P. P. C. Thirty years of luminescent solar concentrator research: Solar energy for the built environment. *Adv. Energy Mater.* **2012**, *2*, 12–35.

[5] Van Sark, W. G. J. H. M. Luminescent solar concentrators–a low cost photovoltaics alternative. *EPJ Web of Conf.* **2012**, *33*, 02003.

[6] Sadeghi, S.; Melikov, R.; Bahmani Jalali, H.; Karatum, O.; Srivastava, S. B.; Conkar, D.; Firat-Karalar, E. N.; Nizamoglu, S. Ecofriendly and efficient luminescent solar concentrators based on fluorescent proteins. *ACS Appl. Mater. Interfaces* **2019**, *11*, 8710–8716.

[7] Yablonovitch, E. Thermodynamics of the fluorescent planar concentrator. *J. Opt. Soc. Amer.* **1980**, *70*, 1362–1363.

[8] Meinardi, F.; McDaniel, H.; Carulli, F.; Colombo, A.; Velizhanin, K. A.; Makarov, N. S.; Simonutti, R.; Klimov, V. I.; Brovelli, S. Highly efficient large-area colourless luminescent solar concentrators using heavy-metal-free colloidal quantum dots. *Nat. Nanotechnol.* **2015**, *10*, 878–885.

[9] Li, H. B.; Wu, K. F.; Lim, J.; Song, H. J.; Klimov, V. I. Doctor-blade deposition of quantum dots onto standard window glass for low-loss large-area luminescent solar concentrators. *Nat. Energy* **2016**, *1*, 16157.

[10] Klimov, V. I.; Baker, T. A.; Lim, J.; Velizhanin, K. A.; McDaniel, H. Quality factor of luminescent solar concentrators and practical concentration limits attainable with semiconductor quantum dots. *ACS Photonics* **2016**, *3*, 1138–1148.

[11] You, Y. M.; Tong, X.; Wang, W. H.; Sun, J. C.; Yu, P.; Ji, H. N.; Niu, X. B.; Wang, Z. M. Eco-friendly colloidal quantum dot-based luminescent solar concentrators. *Adv. Sci.* **2019**, *6*, 1801967.

[12] Sadeghi, S.; Bahmani Jalali, H.; Srivastava, S. B.; Melikov, R.; Baylam, I.; Sennaroglu, A.; Nizamoglu, S. High-performance, large-area, and ecofriendly luminescent solar concentrators using copper-doped InP quantum dots. *iScience* **2020**, *23*, 101272.

[13] Li, Y. X.; Miao, P.; Zhou, W.; Gong, X.; Zhao, X. J. N-doped carbon-dots for luminescent solar concentrators. *J. Mater. Chem. A* **2017**, *5*, 21452–21459.

[14] Li, Z. L.; Zhao, X. J.; Huang, C. B.; Gong, X. Recent advances in green fabrication of luminescent solar concentrators using nontoxic quantum dots as fluorophores. *J. Mater. Chem. C* **2019**, *7*, 12373–12387.

[15] Zhao, H. G.; Zhou, Y. F.; Benetti, D.; Ma, D. L.; Rosei, F. Perovskite quantum dots integrated in large-area luminescent solar concentrators. *Nano Energy* **2017**, *37*, 214–223.

[16] Sadeghi, S.; Bahmani Jalali, H.; Melikov, R.; Kumar, B. G.; Aria, M. M.; Ow-Yang, C. W.; Nizamoglu, S. Stokes-shift-engineered indium phosphide quantum dots for efficient luminescent solar concentrators. *ACS Appl. Mater. Interfaces* **2018**, *10*, 12975–12982.

[17] Meinardi, F.; Colombo, A.; Velizhanin, K. A.; Simonutti, R.; Lorenzon, M.; Beverina, L.; Viswanatha, R.; Klimov, V. I.; Brovelli, S. Large-area luminescent solar concentrators based on 'stokes-shift-engineered' nanocrystals in a mass-polymerized pmma matrix. *Nat. Photonics* **2014**, *8*, 392–399.

[18] Karatum, O.; Jalali, H. B.; Sadeghi, S.; Melikov, R.; Srivastava, S. B.; Nizamoglu, S. Light-emitting devices based on type-II InP/ZnO quantum dots. *ACS Photonics* **2019**, *6*, 939–946.

[19] Wei, M. Y.; De Arquer, F. P. G.; Walters, G.; Yang, Z. Y.; Quan, L. N.; Kim, Y.; Sabatini, R.; Quintero-Bermudez, R.; Gao, L.; Fan, J. Z. et al. Ultrafast narrowband exciton routing within layered perovskite nanoplatelets enables low-loss luminescent solar concentrators. *Nat Energy* **2019**, *4*, 197–205.

[20] Li, Z. L.; Johnston, A.; Wei, M. Y.; Saidaminov, M. I.; De Pina, J. M.; Zheng, X. P.; Liu, J. K.; Liu, Y.; Bakr, O. M.; Sargent, E. H. Solvent-solute coordination engineering for efficient perovskite luminescent solar concentrators. *Joule* **2020**, *4*, 634–643.

[21] Wang, Z.; Yang, W.; Wang, Y. Self-trapped exciton and large stokes shift in pristine and carbon-coated silicon carbide quantum dots. *J. Phys. Chem. C* **2017**, *121*, 20031–20038.

[22] Bailey, R. E.; Nie, S. M. Alloyed semiconductor quantum dots: Tuning the optical properties without changing the particle size. *J. Am. Chem. Soc.* **2003**, *125*, 7100–7106.

[23] Sharma, M.; Gungor, K.; Yeltik, A.; Olutas, M.; Guzelturk, B.; Kelestemur, Y.; Erdem, T.; Delikanli, S.; McBride, J. R.; Demir, H. V. Near-unity emitting copper-doped colloidal semiconductor quantum wells for luminescent solar concentrators. *Adv. Mater.* **2017**, *29*, 1700821.

[24] Bryan, J. D.; Gamelin, D. R. Doped semiconductor nanocrystals: Synthesis, characterization, physical properties, and applications. In *Progress in Inorganic Chemistry*. Karlin, K. D., Ed.; John Wiley & Sons: New York, 2005; pp 47–126.

[25] Viswanatha, R.; Brovelli, S.; Pandey, A.; Crooker, S. A.; Klimov, V. I. Copper-doped inverted core/shell nanocrystals with "permanent" optically active holes. *Nano Lett.* **2011**, *11*, 4753–4758.

[26] Wu, K. F.; Li, H. B.; Klimov, V. I. Tandem luminescent solar concentrators based on engineered quantum dots. *Nat. Photonics* **2018**, *12*, 105–110.

[27] Ma, W. W.; Li, W. J.; Liu, R. Y.; Cao, M. Y.; Zhao, X. J.; Gong, X. Carbon dots and AIE molecules for highly efficient tandem luminescent solar concentrators. *Chem. Commun.* **2019**, *55*, 7486–7489.

[28] Bahmani Jalali, H.; Karatum, O.; Melikov, R.; Dikbas, U. M.; Sadeghi, S.; Yildiz, E.; Dogru, I. B.; Eren, G. O.; Ergun, C.; Sahin, A. et al. Biocompatible quantum funnels for neural photostimulation. *Nano Lett.* **2019**, *19*, 5975–5981.

[29] Bahmani Jalali, H.; Aria, M. M.; Dikbas, U. M.; Sadeghi, S.; Kumar, B. G.; Sahin, M.; Kavakli, I. H.; Ow-Yang, C. W.; Nizamoglu, S. Effective neural photostimulation using indium-based type-II quantum dots. *ACS Nano* **2018**, *12*, 8104–8114.

[30] Bahmani Jalali, H.; Melikov, R.; Sadeghi, S.; Nizamoglu, S. Excitonic energy transfer within InP/ZnS quantum dot Langmuir-Blodgett assemblies. *J. Phys. Chem. C* **2018**, *122*, 11616–11622.
[31] Kumar, B. G.; Sadeghi, S.; Melikov, R.; Aria, M. M.; Jalali, H. B.; Ow-Yang C. W.; Nizamoglu S. Structural control of InP/ZnS core/shell quantum dots enables high-quality white leds. *Nanotechnology* **2018**, *29*, 345605.
[32] Xu, S.; Ziegler, J.; Nann, T. Rapid synthesis of highly luminescent InP and InP/ZnS nanocrystals. *J. Mater. Chem.* **2008**, *18*, 2653–2656.
[33] Dos Remedios, C. G.; Moens, P. D. J. Fluorescence resonance energy transfer spectroscopy is a reliable "ruler" for measuring structural changes in proteins: Dispelling the problem of the unknown orientation factor. *J. Struct. Biol.* **1995**, *115*, 175–185.
[34] Achermann, M.; Petruska, M. A.; Crooker, S. A.; Klimov, V. I. Picosecond energy transfer in quantum dot Langmuir-Blodgett nanoassemblies. *J. Phys. Chem. B* **2003**, *107*, 13782–13787.
[35] Bahmani Jalali, H.; Sadeghi, S.; Sahin, M.; Ozturk, H.; Ow-Yang, C. W.; Nizamoglu, S. Colloidal aluminum antimonide quantum dots. *Chem. Mater.* **2019**, *31*, 4743–4747.
[36] Xie, R. G.; Peng, X. G. Synthesis of Cu-doped InP nanocrystals (d-dots) with ZnSe diffusion barrier as efficient and color-tunable nir emitters. *J. Am. Chem. Soc.* **2009**, *131*, 10645–10651.
[37] Wu, K. F.; Zhu, H. M.; Liu, Z.; Rodríguez-Córdoba, W.; Lian, T. Q. Ultrafast charge separation and long-lived charge separated state in photocatalytic CdS-Pt nanorod heterostructures. *J. Am. Chem. Soc.* **2012**, *134*, 10337–10340.
[38] Dutta, A.; Bera, R.; Ghosh, A.; Patra, A. Ultrafast carrier dynamics of photo-induced Cu-doped CdSe nanocrystals. *J. Phys. Chem. C* **2018**, *122*, 16992–17000.
[39] Peng, P.; Sadtler, B.; Alivisatos, A. P.; Saykally, R. J. Exciton dynamics in CdS–Ag_2S nanorods with tunable composition probed by ultrafast transient absorption spectroscopy. *J. Phys. Chem. C* **2010**, *114*, 5879–5885.
[40] Kramer, I. J.; Levina, L.; Debnath, R.; Zhitomirsky, D.; Sargent, E. H. Solar cells using quantum funnels. *Nano Lett.* **2011**, *11*, 3701–3706.
[41] Klem, E. J. D.; MacNeil, D. D.; Cyr, P. W.; Levina, L.; Sargent, E. H. Efficient solution-processed infrared photovoltaic cells: Planarized all-inorganic bulk heterojunction devices via inter-quantum-dot bridging during growth from solution. *Appl. Phys. Lett.* **2007**, *90*, 183113.
[42] Luther, J. M.; Law, M.; Beard, M. C.; Song, Q.; Reese, M. O.; Ellingson, R. J.; Nozik, A. J. Schottky solar cells based on colloidal nanocrystal films. *Nano Lett.* **2008**, *8*, 3488–3492.
[43] Ruland, A.; Schulz-Drost, C.; Sgobba, V.; Guldi, D. M. Enhancing photocurrent efficiencies by resonance energy transfer in CdTe quantum dot multilayers: Towards rainbow solar cells. *Adv. Mater.* **2011**, *23*, 4573–4577.
[44] Lv, H. J.; Wang, C. C.; Li, G. C.; Burke, R.; Krauss, T. D.; Gao, Y. L.; Eisenberg, R. Semiconductor quantum dot-sensitized rainbow photocathode for effective photoelectrochemical hydrogen generation. *Proc. Natl. Acad. Sci. USA* **2017**, *114*, 11297–11302.
[45] Ministro, J. A study on the synthesis and the optical properties of InP-based quantum dots. Master Degree Thesis, University of Ghent, Belgium, 2014.
[46] Klar, T. A.; Franzl, T.; Rogach, A. L.; Feldmann, J. Super-efficient exciton funneling in layer-by-layer semiconductor nanocrystal structures. *Adv. Mater.* **2005**, *17*, 769–773.
[47] Franzl, T.; Klar, T. A.; Schietinger, S.; Rogach, A. L.; Feldmann, J. Exciton recycling in graded gap nanocrystal structures. *Nano Lett.* **2004**, *4*, 1599–1603.
[48] Rakovich, Y. P.; Gladyshchuk, A. A.; Rusakov, K. I.; Filonovich, S. A.; Gomes, M. J. M.; Talapin, D. V.; Rogach, A. L.; Euchmüller, A. Anti-stokes luminescence of cadmium telluride nanocrystals. *J Appl Spectroscopy* **2002**, *69*, 444–449.
[49] Wang, X. Y.; Yu, W. W.; Zhang, J. Y.; Aldana, J.; Peng, X. G.; Xiao, M. Photoluminescence upconversion in colloidal CdTe quantum dots. *Phys. Rev. B* **2003**, *68*, 125318.
[50] Rogach, A. L.; Klar, T. A.; Lupton, J. M.; Meijerink, A.; Feldmann, J. Energy transfer with semiconductor nanocrystals. *J. Mater. Chem.* **2009**, *19*, 1208–1221.
[51] Förster, T. Zwischenmolekulare energiewanderung und fluoreszenz. *Ann. Phys.* **1948**, *437*, 55–75.
[52] Trofymchuk, K.; Reisch, A.; Didier, P.; Fras, F.; Gilliot, P.; Mely, Y.; Klymchenko, A. S. Giant light-harvesting nanoantenna for single-molecule detection in ambient light. *Nat. Photonics* **2017**, *11*, 657–663.